Information Fusion 14 (2013) 396–409

Contents lists available at SciVerse ScienceDirect

Information Fusion

journal homepage: www.elsevier.com/locate/inffus

Full Length Article

Space-variant blur deconvolution and denoising in the dual exposure problem

Miguel Tallón [a], Javier Mateos [a,*], S. Derin Babacan [b], Rafael Molina [a], Aggelos K. Katsaggelos [c]

[a] Dept. de Ciencias de la Computación e I.A., Universidad de Granada, Granada, Spain
[b] Beckman Institute, University of Illinois at Urbana–Champaign, IL, USA
[c] Dept. of Electrical Engineering & Computer Science, Northwestern University, Evanston, IL, USA

ARTICLE INFO

Article history:
Received 24 January 2012
Received in revised form 15 July 2012
Accepted 8 August 2012
Available online 28 August 2012

Keywords:
Blind deconvolution
Motion blur
Low light imaging
Image fusion
Image denoising

ABSTRACT

In this paper we propose a space-variant blur estimation and effective denoising/deconvolution method for combining a long exposure blurry image with a short exposure noisy one. The blur in the long exposure shot is mainly caused by camera shake or object motion, and the noise in the underexposed image is introduced by the gain factor applied to the sensor when the ISO is set to an high value. Due to the space variant degradation, the image pair is divided into overlapping patches for processing. The main idea in the deconvolution algorithm is to incorporate a combination of prior image models into a spatially-varying deblurring/denoising framework which is applied to each patch. The method employs a kernel and parameter estimation method to choose between denoising or deblurring each patch. Experiments on both synthetic and real images are provided to validate the proposed approach.

1. Introduction

The removal of the blur caused by camera shake and object motion is still a challenging problem, even more when images are taken in dim environments or when the sensors are too small to capture enough photons of a scene as common with in mobile phone cameras. A long exposure time is required in these situations. However, any motion of the camera during the long exposure causes significant blurring in the the recorded image. Using a tripod can remove the camera shake but it is not useful when there are moving objects in the scene; furthermore it is not practical and cumbersome to use in many cases. Some hardware-based solutions attempt to reduce the blur in long exposure shots by increasing the sensor gain (ISO parameter) which leads to noise amplification, or by opening the aperture at the expense of a smaller depth of field. Additionally, many digital cameras incorporate optical image stabilizers which may help to reduce camera shake.

Unfortunately, none of these solutions are sufficient in dim environments and especially with dynamic scenes with moving objects. A possible solution is to apply single image blind deconvolution on the long exposure image. However, this is a challenging problem with a number of problems to be addressed including spatially-varying blur, and saturated pixels. Utilizing an accompanying short exposure image for the deconvolution provides valuable information that significantly improves the restoration. Although this additional image contains accurate information about image edges, it is generally contaminated with a high level of noise and color information might be lost. Since both images do not have the same output levels, and may not be taken at exactly the same moment, a misalignment is likely to appear between the images and hence the image pair must be photometrically and geometrically calibrated.

A number of methods have been developed that use different exposed image pairs for blind deconvolution [1–3]. In [1], the long-exposure image and the denoised version of the short-exposure image are utilized to estimate a sharp kernel. However, accurate knowledge of the noise variance in the short exposure image is necessary to apply the denoising method, since an inaccurate noise variance could cause over-smoothing and over-suppression of details. A Bayesian framework to model the unknown image and blur, as well as the parameters associated to the models, is proposed in [2,3]. Using this framework, image, blur and parameters are estimated without user intervention. In [3], a procedure to combine three observation models corresponding to the long exposure image, the short exposure image and a combination of the long and short exposure image model is proposed. All these previous works assume a space-invariant blur, which seldom occurs in practice. It has been lately shown that even the optical system of the camera generates significant space-variant blur [4]. The assumption of invariant blur might lead to significant artifacts in some regions. Recent works [5–7] attempt to overcome this limitation by introducing a more sophisticated non-uniform kernel

* Corresponding author.
E-mail addresses: mtallon@decsai.ugr.es (M. Tallón), jmd@decsai.ugr.es (J. Mateos), dbabacan@illinois.edu (S.D. Babacan), rms@decsai.ugr.es (R. Molina), aggk@eecs.northwestern.edu (A.K. Katsaggelos).

1566-2535/$ - see front matter © 2012 Elsevier B.V. All rights reserved.
http://dx.doi.org/10.1016/j.inffus.2012.08.003

modeling. In [5], the authors use a single kernel to develop a parametrically non-uniform blur which allows a wider class of blurs to be modeled, but it is only applicable to static scenes. In [6,7] space-variant blur modeling and estimation are utilized. The images are divided into patches and independent blur kernels are estimated for each patch. The deconvolution process in [6] was improved in [7] by incorporating a term taking into account the short exposure image. The restored images obtained in [6,7] can suffer from blocking artifacts in adjacent patches due to blur changes, and furthermore, all model parameters have to be selected manually.

Image fusion methods are proposed in [8–10]. The method in [8] classifies the pixels in both images as blurry or sharp, and fuses them by a linear combination. In a more recent work [9], the authors propose an algorithm that can be applied to a set of images with different exposure times taken by mobile cameras. The algorithm aims at obtaining a (probably blurred) high dynamic range (HDR) image and then fusing it with a noisy image. It uses wavelet decomposition to select, at each scale and orientation, the information from the HDR image to be included in the noisy one. In [10], an image fusion algorithm is described based on the idea of quantifying the importance of regions and fusing them according to some metrics, such as contrast, size, and shape of region.

In this paper, we propose a new method[1] to combine a long exposure blurry image with a short exposure noisy one to obtain a sharp restoration that is both noiseless and free of blur. The developed method is suitable for both camera shake and moving objects blurs. First, we divide the input images in overlapping patches and estimate the blur kernel in each patch. We then employ a Bayesian fully-automatic procedure which combines two image priors to estimate the unknown image from the estimated kernels and the observed image pair.

When blur estimate is not sufficiently accurate due to, for instance, object motion or weak textures in the patch, the algorithm may fail to correctly apply deconvolution on the patch. We developed a method to detect such cases and correct them by using instead a denoised version of the short exposure patch. Finally, the estimation of the overlapped patches is combined using a windowing function to obtain a restoration without blocking artifacts. Experimental results demonstrate that the proposed approach provides both high quality space variant blur and image estimates even in challenging datasets.

The rest of this paper is organized as follows. In Section 2 we describe in detail each stage of our algorithm. Synthetic and real experiments are compared and depicted in Section 3. Finally conclusions are drawn in Section 4.

2. Proposed algorithm

Our approach to space-variant deblurring is summarized in the following algorithm.

Algorithm 1. Main Algorithm

Preprocessing: image pair calibration and division in patches. (Sec. 2.1)
for *each patch* **do**
  Perform kernel estimation (Sec. 2.2)
  Deconvolve/denoise the patch (Sec. 2.3)
end
Postprocessing: Blend the restored patches to form the final image (Sec. 2.5)

The images are represented in the YC_bC_r colorspace. The restoration method is applied only on the luminance component and the restoration is fused with the chrominance component of the blurred image. In the present paper, we assume that the blurred image captured under dim conditions is correctly exposed (i.e., there is no saturated pixels) and, hence, its color information is preserved. If that were not the case, we could use the color information from the noisy image where reliable. The stages of the algorithm are explained in detail in the following sections.

2.1. Preprocessing

As mentioned before, the image pair with different exposure conditions must be photometrically and geometrically registered. For photometric calibration, we apply histogram equalization [12] on the luminance of the short-exposure image using the histogram of the long-exposure image. Histogram equalization technique is suitable for our purpose since it works with accumulative histograms, neglecting the geometry of the scene.

Once both images are photometrically calibrated, we proceed with the geometric calibration. This is performed by first extracting Surf features [13] from both images and removing the outliers using RANSAC [14], and then computing the homography matrix with the DLT [15] algorithm to finally stitch the images. The quality of the restoration highly depends on the accuracy of this stage.

Next, we divide the images into overlapping patches, which allows us to model a space-variant kernel, computing a different kernel function per patch. This framework also helps us to improve the memory allocation and computation speed, since it utilizes blocks of reduced size. The block size $B_x \times B_y$ in horizontal and vertical directions are computed as

$$B_z = \left\lfloor \frac{N_z}{(1-overlap)p_z + overlap} \right\rfloor, \quad z \in \{x, y\},$$

with N_x and N_y the size of the images in horizontal and vertical dimensions, $0 \leqslant overlap < 1$ is the overlapping factor and p_x and p_y are the number of patches in the horizontal and vertical directions, respectively. For instance, for an image of size $N_y = 800$, $N_x = 600$ pixels, with a number of patches $p_y = 8$ and $p_x = 6$ and a overlap percentage of 50% ($overlap = 0.5$), the block size is $B_y = 177$ and $B_x = 171$.

2.2. Kernel estimation

Once the observations have been calibrated and divided into patches, we assume a linear and space-invariant degradation model as in [2], so that the observation process of each patch p of each image can be mathematically expressed in matrix–vector notation as

$$\mathbf{y}_1^p = \mathbf{H}^p \mathbf{x}^p + \mathbf{n}_1, \tag{1}$$
$$\mathbf{y}_2^p = \mathbf{x}^p + \mathbf{n}_2, \tag{2}$$

where $\mathbf{y}_1^p$ and $\mathbf{y}_2^p$ are the $B_y \times B_x$ observed long- and short-exposure image patches, respectively, represented as column vectors of size $(B_y \times B_x) \times 1$. The unknown original image patch is $\mathbf{x}^p$, $\mathbf{H}^p$ is the unknown $(B_y \times B_x) \times (B_y \times B_x)$ space-invariant blur convolution matrix, and $\mathbf{n}_1$ and $\mathbf{n}_2$ are assumed to be zero mean white Gaussian noise components.

[1] Preliminary results of this work were presented at Internal Symposium on Image and Signal Processing and Analysis (ISPA), 2011 [11].

The space-variant kernel is estimated per patch from the observed patches $\mathbf{y}_1^p$ and $\mathbf{y}_2^p$ where $p = (p_1, p_2)$ with $1 \leqslant p_1 \leqslant p_y$ and $1 \leqslant p_2 \leqslant p_x$. Thus the matrix $\mathbf{Y}_2^p$ represents the image patch $\mathbf{y}_2^p$ written as a $(B_y \times B_x) \times (h_y \times h_x)$ convolution matrix, where the blur size (h_y, h_x) is provided by the user and finally, $\mathbf{h}^p$ represents the blur kernel in patch p.

Using (1) and (2), the estimate $\hat{\mathbf{h}}^p$ of a kernel $\mathbf{h}^p$ is found by solving

$$\hat{\mathbf{h}}^p = \arg\min_{\mathbf{h}^p} \|\mathbf{y}_1^p - \mathbf{Y}_2^p \mathbf{h}^p\|^2, \tag{3}$$

subject to the constraints $0 \leqslant \mathbf{h}_i^p \leqslant 1,\ \sum_i \mathbf{h}_i^p = 1,\ i = 1, \ldots, (h_x \times h_y)$. This problem can easily be solved using a constrained linear least-squares solver (we used the `lsqlin` routine implemented in MATLAB). The boundary problem in the convolutions is solved by using the image values in the neighboring patches, when available, or by replicating the pixel values in the patch boundaries for the image borders.

Kernel estimation may fail in patches with weak texture or saturated pixels, i.e., when there is not enough available information for the kernel estimation. The estimates will also be unreliable in patches with mixed blur, such as patches with moving objects or with objects at different distances. Several kernel correction algorithms have been proposed to address these problems (see, e.g., [6] or [16]). In this paper, instead of correcting the estimating kernels, we take an alternative approach: The proposed deconvolution algorithm is able to provide information that can be used to determine if the patch was successfully deconvolved using the estimated kernel. This information helps us to make our method robust to poor blur estimates (Section 2.4) and, in cases where the deconvolved patch is not of sufficient quality, we obtain a better patch estimate by denoising the noisy short exposure image patch.

2.3. Deconvolution

Once the kernel for each patch has been estimated, we need to obtain accurate estimates of the image for each patch. For this purpose, we adopt the principle of model combination to develop a Bayesian deconvolution algorithm for the dual exposure problem.

The key idea consists of modeling the unknown image within a hierarchical Bayesian formulation using a combination of a sparse and a non-sparse prior image. Specifically, we use the combination of a Total Variation (TV) model [17] with a simultaneous autoregressive (SAR) prior [18]. The idea of model combination has been successfully utilized also in other areas, such as image restoration [19], super-resolution [20] or image decomposition [21].

The goal behind the model combination is to preserve as many details as possible from both observations by incorporating the advantages of TV and SAR image models together. The TV image model has a good edge preservation capability but tends to smooth out textured areas, whereas the SAR model preserves the textures better but sharp transitions such as the image edges are oversmoothed. Our goal is to preserve both the texture and the sharp edges by combining both models. We provide a description of the individual prior distributions used to model the unknowns in the following.

The TV image prior is given by

$$p_1(\mathbf{x}^p|\alpha_1^p) \propto (\alpha_1^p)^{B/2} \exp\left[-\alpha_1^p \sum_{j=1}^{B} \sqrt{\left(\Delta_j^u(\mathbf{x}^p)\right)^2 + \left(\Delta_j^v(\mathbf{x}^p)\right)^2}\right], \tag{4}$$

where $j = 1, \ldots, B$, α_1^p is the model parameter, and the operators $\Delta_j^u(\mathbf{x})$ and $\Delta_j^v(\mathbf{x})$ correspond to horizontal and vertical first order differences at pixel j, respectively. The non-sparse SAR model is defined as

$$p_2(\mathbf{x}^p|\alpha_2^p) \propto (\alpha_2^p)^{B/2} \exp\left[-\frac{\alpha_2^p}{2}\|\mathbf{C}\mathbf{x}^p\|^2\right], \tag{5}$$

where $\mathbf{C}$ is the Laplacian operator and α_2^p is the model parameter. Notice that in principle we could have considered a single prior model, combination of the two above, of the form

$$p(\mathbf{x}^p|\alpha_1^p, \alpha_2^p) = \frac{1}{Z(\alpha_1^p, \alpha_2^p)} \times \exp\left[-\alpha_1^p \sum_{j=1}^{B} \sqrt{\left(\Delta_j^u(\mathbf{x}^p)\right)^2 + \left(\Delta_j^v(\mathbf{x}^p)\right)^2} - \frac{\alpha_2^p}{2}\|\mathbf{C}\mathbf{x}^p\|^2\right]. \tag{6}$$

However, the estimation of the parameters is very hard for this image prior model, since the partition function $Z(\alpha_1^p, \alpha_2^p)$ is unknown and difficult to approximate.

From (1) and (2), and assuming that the noise $\mathbf{n}_1^p$ and $\mathbf{n}_2^p$ follow independent Gaussian distributions of zero mean and variances $(\beta_1^p)^{-1}$ and $(\beta_2^p)^{-1}$, respectively, we write the conditional probability distribution of the observations as

$$p(\mathbf{y}_1^p, \mathbf{y}_2^p|\mathbf{x}^p, \beta_1^p, \beta_2^p) \propto (\beta_1^p)^{B/2} (\beta_2^p)^{B/2} \times \exp\left[-\frac{\beta_1^p}{2}\|\mathbf{y}_1^p - \mathbf{H}^p\mathbf{x}^p\|^2 - \frac{\beta_2^p}{2}\|\mathbf{y}_2^p - \mathbf{x}^p\|^2\right], \tag{7}$$

where $B = B_y \times B_x$ is the patch size.

The proposed prior combination and observation model depend on a set of parameters whose values have to be estimated together with the image. For their modeling we employ improper non informative priors, $p(\xi) \propto \text{const},\ \xi \in \{\alpha_1^p, \alpha_2^p, \beta_1^p, \beta_2^p\}$, over $(0, \infty)$.

Finally, combining the observation model Eq. (7) and the non informative priors for the parameters with the priors models in Eqs. (4) and (5) we obtain the joint probability distributions

$$p_1(\Omega, \alpha_1, \mathbf{y}_1^p, \mathbf{y}_2^p) = p(\mathbf{x}^p|\alpha_1^p)p(\alpha_1^p)p(\mathbf{y}_1^p, \mathbf{y}_2^p|\Omega)p(\beta_1^p)p(\beta_2^p), \tag{8}$$

$$p_2(\Omega, \alpha_2, \mathbf{y}_1^p, \mathbf{y}_2^p) = p(\mathbf{x}^p|\alpha_2^p)p(\alpha_2^p)p(\mathbf{y}_1^p, \mathbf{y}_2^p|\Omega)p(\beta_1^p)p(\beta_2^p), \tag{9}$$

where $\Omega = \{\mathbf{x}^p, \beta_1^p, \beta_2^p\}$.

This joint distribution is used to estimate both the unknown image patches $\mathbf{x}^p$ and all algorithmic parameters. In this work, we employ a variational approach to obtain an approximation of the posterior distribution of the image patch and the parameters, which is described next. Let us denote by Θ the set of unknowns, i.e., $\Theta = \{\Omega, \alpha_1^p, \alpha_2^p\}$. The goal is to approximate the posterior distribution $p(\Theta|\mathbf{y}_1^p, \mathbf{y}_2^p)$ by another distribution $q(\Theta)$ which allows a tractable analysis. Generally, the only assumption made in variational Bayesian analysis is that the approximating distribution $q(\Theta)$ is factorizable. In this work, we use the following factorization:

$$q(\Theta) = q(\Omega)q(\alpha_1^p)q(\alpha_2^p), \tag{10}$$

with $q(\Omega) = q(\mathbf{x}^p)q(\beta_1^p)q(\beta_2^p)$. The approximating distribution $q(\Theta)$ is then found by minimizing the Kullback–Leibler (KL) divergence between $q(\Theta)$ and $p(\Theta|\mathbf{y}_1^p, \mathbf{y}_2^p)$, which is given by

$$\hat{q}(\Theta) = \arg\min_{q(\Theta)} \sum_{k=1}^{2} \lambda_k\ C_{KL}(q(\Omega)q(\alpha_k^p)\|p_k(\Omega, \alpha_k^p|\mathbf{y}_1^p, \mathbf{y}_2^p)), \tag{11}$$

with $\lambda_k \geqslant 0$, $\lambda_1 + \lambda_2 = 1$, and the KL divergence [22] given by

$$C_{KL}\left(q(\Omega)q(\alpha_k^p)\|p_k(\Omega,\alpha_k^p|\mathbf{y}_1^p,\mathbf{y}_2^p)\right) = \int q(\Theta)\log\left(\frac{q(\Omega)q(\alpha_k^p)}{p_k(\Omega,\alpha_k^p,\mathbf{y}_1^p,\mathbf{y}_2^p)}\right)d\Theta + \text{const}, \quad \text{for } k=1,2. \tag{12}$$

The estimation of λ_1 and λ_2 will not be addressed in this paper but we will show experimentally that a non-degenerate combination of divergences (e.g., $0<\lambda_1<1$) provides better results than either $\lambda_1=0$ or $\lambda_1=1$.

The expression in (11) can be rewritten as

$$\hat{q}(\Theta) = \arg\min_{q(\Theta)} \int q(\Theta) \times \log\left(\frac{q(\Omega)}{p(\mathbf{y}_1^p,\mathbf{y}_2^p|\Omega)p(\beta_1^p)p(\beta_2^p)}\prod_{k=1}^{2}\left[\frac{q(\alpha_k^p)}{p_k(\mathbf{x}^p|\alpha_k^p)p(\alpha_k^p)}\right]^{\lambda_k}\right)d\Theta. \tag{13}$$

Unfortunately, the variational Bayesian analysis cannot be directly utilized with the image prior used in this work, since the TV prior leads to an integral in (13) which cannot be calculated. The problems caused by the TV prior can be avoided by utilizing a majorization–minimization (MM) approach, whose details are given in [17]. This method finds a bound for the distribution in Eq. (4) and makes the analytical derivation of the Bayesian inference tractable. Here we also employ this approach for inference, and provide an outline in the following.

Let us consider the functional $\mathbf{M}(\alpha_1^p,\mathbf{x}^p,\mathbf{w}^p)$, where $\mathbf{w}^p\in(R^+)^B$ is a B-dimensional vector and components w_j, $j=1,\ldots,B$,

$$\mathbf{M}(\alpha_1^p,\mathbf{x}^p,\mathbf{w}^p) = (\alpha_1^p)^{B/2} \times \exp\left[-\frac{\alpha_1^p}{2}\sum_{j=1}^{B}\frac{\left(\Delta_j^u(\mathbf{x}^p)\right)^2+\left(\Delta_j^v(\mathbf{x}^p)\right)^2+w_j}{\sqrt{w_j}}\right]. \tag{14}$$

The auxiliary vector $\mathbf{w}^p$ needs to be computed simultaneously with the image and has a direct relation with the gradients of the latent image patch $\mathbf{x}^p$. It can be shown (see [17] for the details) that the functional $\mathbf{M}(\alpha_1^p,\mathbf{x}^p,\mathbf{w}^p)$ is a lower bound of the image prior $p_1(\mathbf{x}^p|\alpha_1^p)$, that is:

$$p_1(\mathbf{x}^p|\alpha_1^p) \geqslant \mathbf{M}(\alpha_1^p,\mathbf{x}^p,\mathbf{w}^p). \tag{15}$$

Using Eq. (15), a lower bound of the joint probability distributions in Eq. (9) can be found, that is:

$$p_1(\Omega,\alpha_1^p,\mathbf{y}_1^p,\mathbf{y}_2^p) \geqslant \mathbf{M}(\alpha_1^p,\mathbf{x}^p,\mathbf{w}^p)p(\alpha_1^p)p(\mathbf{y}_1^p,\mathbf{y}_2^p|\Omega)p(\beta_1^p)p(\beta_2^p) = \mathbf{F}(\Omega,\alpha_1^p,\mathbf{w}^p,\mathbf{y}_1^p,\mathbf{y}_2^p), \tag{16}$$

which leads to the following upper bound for the KL divergence in Eq. (12)

$$C_{KL}\left(q(\Omega)q(\alpha_1^p)\|p_1(\Omega,\alpha_1^p,\mathbf{y}_1^p,\mathbf{y}_2^p)\right) \leqslant \min_{\mathbf{w}^p} C_{KL}\left(q(\Omega)q(\alpha_1^p)\|\mathbf{F}(\Omega,\alpha_1^p,\mathbf{w}^p,\mathbf{y}_1^p,\mathbf{y}_2^p)\right). \tag{17}$$

Before we proceed to calculate the approximation to the posterior distribution, we first observe that to calculate $q(\alpha_k)$, $k=1,2$, we only have to take into account the divergence where that distribution appears. Thus, we can write

$$q(\alpha_1^p) = \text{const}\times\exp(\langle\log\mathbf{F}(\Omega,\alpha_1^p,\mathbf{w}^p,\mathbf{y}_1^p,\mathbf{y}_2^p)\rangle_\Omega), \tag{18}$$

$$q(\alpha_2^p) = \text{const}\times\exp(\langle\log p_2(\Omega,\alpha_2^p,\mathbf{y}_1^p,\mathbf{y}_2^p)\rangle_\Omega), \tag{19}$$

where $\langle\cdot\rangle_\Omega = \mathbf{E}_{q(\Omega)}[\cdot]$, the expectation with respect to the distribution $q(\Omega)$.

Furthermore, to calculate the rest of the distributions, $q(\omega)$, $\omega\in\Omega$, we have to take into account both divergences, obtaining

$$q(\omega) = \text{const}\times\exp\left(\left\langle\log p(\mathbf{y}_1^p,\mathbf{y}_2^p|\Omega)p(\beta_1^p)p(\beta_2^p)\times\left[\mathbf{M}(\alpha_1^p,\mathbf{x}^p,\mathbf{w}^p)p(\alpha_1^p)\right]^{\lambda}\left[p_2(\mathbf{x}^p|\alpha_2^p)p(\alpha_2^p)\right]^{1-\lambda}\right\rangle_{\Omega_\omega}\right), \tag{20}$$

where Ω_ω denotes the set of unknown with ω removed, and $\lambda=\lambda_1$ and, hence, $\lambda_2=1-\lambda$.

Calculating the above distributions for each unknown results in an iterative procedure, which converges to the best approximation of the true posterior distribution $p(\Theta|\mathbf{y}_1^p,\mathbf{y}_2^p)$ by distributions of the form in Eq. (11). In this work, we utilize the means of these distributions as the point estimates of the unknowns. Let us now make explicit the form of each of these distributions.

The distribution $q(\mathbf{x}^p)$ is calculated from Eq. (20) as the multivariate Gaussian distribution $q(\mathbf{x}^p)=\mathcal{N}(\mathbf{x}^p|\langle\mathbf{x}^p\rangle,\Sigma_{\mathbf{x}}^p)$ where its mean and covariance matrix are given by

$$\langle\mathbf{x}^p\rangle = \Sigma_{\mathbf{x}}^p\left(\langle\beta_1^p\rangle(\mathbf{H}^p)^t\mathbf{y}_1^p + \langle\beta_2^p\rangle\mathbf{y}_2^p\right), \tag{21}$$

$$(\Sigma_{\mathbf{x}}^p)^{-1} = \lambda\langle\alpha_1^p\rangle((\Delta^u)^t\mathbf{W}^p\Delta^u + (\Delta^v)^t\mathbf{W}^p\Delta^v) + (1-\lambda)\langle\alpha_2^p\rangle\mathbf{C}^t\mathbf{C} + \langle\beta_1^p\rangle(\mathbf{H}^p)^t\mathbf{H}^p + \langle\beta_2^p\rangle\mathbf{I}, \tag{22}$$

where Δ^u and Δ^v are the discrete approximations to the gradient operator in the horizontal and vertical directions, respectively, $\mathbf{W}^p$ is the $B\times B$ diagonal matrix of the form $\mathbf{W}^p = diag\left(\left(w_j^p\right)^{-\frac{1}{2}}\right)$, for $j=1,\ldots,B$ with

$$w_j^p = \left\langle(\Delta_j^u(\mathbf{x}^p))^2 + \left(\Delta_j^v(\mathbf{x}^p)\right)^2\right\rangle, \quad j=1,\ldots,B. \tag{23}$$

The matrix $\mathbf{W}^p$ can be interpreted as a spatially varying weighting matrix that provides spatial adaptivity to the model controlling the amount of smoothing at each pixel location depending on the intensity variation at that pixel. The parameter λ controls the contribution from each prior model. The value of $\lambda=0$ leads to the classical SAR restoration model while $\lambda=1$ leads to the TV restoration model. A sensible combination of both models allows to recover the textures of the image while preserving sharp edges [19].

The rest of parameter estimates are found as the means of the distributions from Eqs. (18)–(20) given by

$$\langle\alpha_1^p\rangle = \frac{B}{2\sum_{j=1}^{B}\sqrt{w_j^p}}, \tag{24}$$

$$\langle\alpha_2^p\rangle = \frac{B}{\langle\|\mathbf{C}\mathbf{x}^p\|^2\rangle}, \tag{25}$$

$$\langle\beta_1^p\rangle = \frac{B}{\left\langle\|\mathbf{y}_1^p-\mathbf{H}^p\mathbf{x}^p\|^2\right\rangle}, \tag{26}$$

$$\langle\beta_2^p\rangle = \frac{B}{\left\langle\|\mathbf{y}_2^p-\mathbf{x}^p\|^2\right\rangle}. \tag{27}$$

The explicit forms of the expectations above are given by

$$\left\langle\left(\Delta_j^u(\mathbf{x}^p)\right)^2+\left(\Delta_j^v(\mathbf{x}^p)\right)^2\right\rangle = \left(\Delta_j^u(\langle\mathbf{x}^p\rangle)\right)^2+\left(\Delta_j^v(\langle\mathbf{x}^p\rangle)\right)^2 + \text{trace}\left(((\Delta^u)^t\Delta^u+(\Delta^v)^t\Delta^v)\Sigma_{\mathbf{x}}^p\right), \tag{28}$$

$$\langle\|\mathbf{C}\mathbf{x}^p\|^2\rangle = \|\mathbf{C}\langle\mathbf{x}^p\rangle\|^2 + \text{trace}\left(\mathbf{C}^t\mathbf{C}\Sigma_{\mathbf{x}}^p\right), \tag{29}$$

$$\left\langle\|\mathbf{y}_1^p-\mathbf{H}^p\mathbf{x}^p\|^2\right\rangle = \left\|\mathbf{y}_1^p-\mathbf{H}^p\langle\mathbf{x}^p\rangle\right\|^2 + \text{trace}\left(\mathbf{H}^t\mathbf{H}\Sigma_{\mathbf{x}}^p\right), \tag{30}$$

$$\left\langle\left\|\mathbf{y}_2^p-\mathbf{x}^p\right\|^2\right\rangle = \left\|\mathbf{y}_2^p-\langle\mathbf{x}^p\rangle\right\|^2 + \text{trace}\left(\Sigma_{\mathbf{x}}^p\right). \tag{31}$$

To simplify the calculations we assume, for the estimation of the parameters, that the distribution on $\mathbf{x}^p$ is a degenerate distribution

and, hence, the expectations in (28)–(31) can be calculated without taking into account the contribution of the corresponding traces.

To select the best value of λ we find estimates of the image patch $\mathbf{x}^p$ by varying λ from 0 to 1 in steps of 0.1, and select the value of λ, and the restoration $\mathbf{x}^p_\lambda$, that minimizes $\left\|\mathbf{y}^p_1 - \mathbf{H}^p\mathbf{x}^p_\lambda\right\|^2$.

The overall iterative procedure is summarized in Algorithm 1. Using the initial image estimate $\mathbf{x}^p = \mathbf{y}^p_1$, the algorithm alternates between the estimation of the parameters using (23)–(27) and estimating the image patches $\mathbf{x}^p$ by solving (21) using the conjugate gradient method to avoid the explicit computation of $\mathbf{\Sigma}^p_{\mathbf{x}}$.

Algorithm 1. Proposed Deconvolution Method.

Inputs: $\mathbf{y}^p_1, \mathbf{y}^p_2$ the long- and short-exposure images patches, respectively; and $\mathbf{h}^p$ the kernel estimated for patch p.
Output: $\mathbf{x}^p$ the restored patch.

for $\lambda = 0$ *to* 1 *in steps of* 0.1 **do**
  Set $\mathbf{x}^p_{new} = \mathbf{y}^p_1$
  repeat
    Set $\mathbf{x}^p_{old} = \mathbf{x}^p_{new}$
    Find the estimation of the parameters using Eqs. (23)-(27) with $\mathbf{x}^p = \mathbf{x}^p_{old}$
    Find $\mathbf{x}^p_{new}$, the new image patch estimate using Eq. (21)
  until $\frac{\|\mathbf{x}^p_{new} - \mathbf{x}^p_{old}\|^2}{\|\mathbf{x}^p_{old}\|^2} \leq threshold$
  Set $\mathbf{x}^p_\lambda = \mathbf{x}^p_{new}$
end
Set $\mathbf{x}^p = \text{argmin}_{\mathbf{x}^p_\lambda} \| \mathbf{y}^p_1 - \mathbf{H}^p\mathbf{x}^p_\lambda \|^2$

2.4. Robustness to poor blur estimates

The proposed deconvolution method results in high-quality estimates if the blur is invariant within each patch. However, as other deconvolution algorithms, it may fail to accurately estimate the image if blur estimate is not precise. As mentioned before, this problem may occur in weak textured patches with not enough structural information, and in patches where the blur varies across the patch, such as areas with moving objects or multiple objects at different distances.

To overcome these problems, we select for each patch either the deconvolution result provided by Algorithm 1 or a denoised version of the noisy patch $\mathbf{y}^p_2$. Due to the short exposure time, it is expected that the image $\mathbf{y}^p_2$ will not be affected by motion blur. As a result, better image estimates can be obtained by denoising $\mathbf{y}^p_2$ than by deconvolving $\mathbf{y}^p_1$ in areas with inaccurate kernel estimations. However, as will be shown in the experiment section, denoising the whole image does not provide accurate enough results. This is because many details are lost during denoising in regions with high spatial activity due to the high amount of noise.

In patches where the blur estimates are poor, the deconvolved patch will be quite different from the original one and the estimation of β^p_2 (the noise precision in the short exposure image) generally results in an extremely small value. We utilize this information to decide between deconvolving or denoising the patches. Specifically, we compute the mean value $\bar{\beta}^p_2$ of the estimates of β^p_2 for all the patches, and apply denoising in all patches where $t * \beta^p_2$ is smaller than this mean value. In our experiments we found that $t = 1.5$ is an appropriate value. Denoising is performed by the BM3D method in [23]. This method requires the estimation of the noise variance which is obtained as the mean value of $\beta^{p^{-1}}_2$ for all the blocks where deblurring is selected, that is, not taking into account the patches where $t * \beta^p_2 < \bar{\beta}_2$.

It should be emphasized, however, that a poor blur estimation does not necessarily lead to a poor deconvolved patch, since the deconvolution process takes into account both long and short exposure patches. Hence, it may compensate for a poor blur estimate by giving priority to the information from the short exposure patch. However, patches with a value of β^p_2 much smaller than the mean value $\bar{\beta}_2$ are always poorly deconvolved patches and therefore substituting them by the denoised version of the patch $\mathbf{y}^p_2$ improves the restoration quality.

2.5. Postprocessing

After all image patches are processed, we merge the restored patches using a normalized windowing function $\mathbf{s}$ to avoid blocking artifacts as

$$\mathbf{x} = \sum_p^P \mathbf{s}^p\mathbf{x}^p, \tag{32}$$

$$\sum_p^P \mathbf{s}^p_l = 1 \leqslant (N_x \times N_y), \tag{33}$$

with P the number of patches. A number of windowing functions can be used (Gaussian, rectangular and Hann). Empirically, we found that a Hann window function over each patch provided the best results, which was also successfully utilized in [24].

3. Experiments

In this section, we analyze the performance of the developed algorithm on synthetic and real image pairs acquired in dim environments with different digital cameras. In order to generate a synthetic dataset, we divide the images into non overlapping patches and apply a locally invariant blurring function to each block which leads to a globally variant blur. The objective of this experiment is, assuming a locally invariant but globally variant kernel, to evaluate both the kernel estimation and the accuracy of the deconvolution algorithm. Note that the deconvolution procedure exploits information from both the blurred and short exposure images.

A set of blurred images simulating long exposure shots are obtained as follows. The original image, depicted in Fig. 1a, of size 800×600, was divided in 4×3 non-overlapping patches. We generated four different blurred images, shown in the top row of Fig. 2, by convolving each one of the original image patches with the four different set of kernels, depicted in Fig. 2. Each blur kernel is of size 15×15.

In order to simulate a realistic under-exposed image, we follow the image acquisition pipeline described in [25] and simulate the under-exposure corruption in the irradiance domain. First, the original image in Fig. 1a was converted into the irradiance domain by undoing the gamma correction using $\gamma = 2.2$. Then, we assumed that the short exposure image had an exposure value (EV) six steps

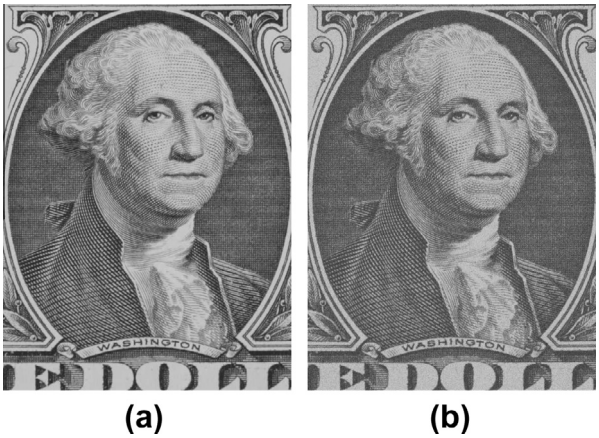

Fig. 1. (a) Original image, (b) simulated short-exposure image calibrated to the image in Fig. 2c.

lower than the original image and divided each pixel value by 64. Gaussian noise corresponding to a signal-to-noise-ratio (SNR) of 10 dB was added to simulate the camera noise. The resulting image was then gamma corrected and a quantization to eight bits was applied to obtain the under-exposed image. Finally, the images are photometrically calibrated using histogram equalization with the histogram of the corresponding blurred image. The obtained noisy observation, calibrated with the histogram of the blurred image in Fig. 2c, is depicted in Fig. 1b.

The proposed method was run using *threshold* = 10^{-5} to stop the iterative procedure in Algorithm 1. The estimated kernels are plotted in the last row of Fig. 3. It is clear that the proposed method accurately recovers the blurring kernels. This was expected since each block contains a single, space-invariant blur and, hence, none of the deblurred patches were replaced by their denoised versions in any of the four synthetic experiments. To obtain the best possible restoration results, depicted in the first row of Fig. 3, the value λ was adjusted, varying λ from 0 to 1 in steps of 0.1, to its optimal value (in PSNR) for each block. The results when the values of λ are estimated using the proposed algorithm are shown in the second row of Fig. 3. Examining both results it is difficult to find any differences except that the restorations obtained with the optimal values of λ seems to be slightly sharper. The optimal and estimated values of λ for each patch in Fig. 3c are shown in Table 3. As is clear from the table, both estimated and optimal values are quite close, which confirms that the proposed estimation method for λ is accurate.

We compared the proposed algorithm with pure denoising using the method in [23], the Richardson–Lucy (RL) based blind deconvolution method, implemented by `deconvblind` routine in MATLAB, and a state-of-the-art dual exposure blind deconvolution presented in [2]. All of these deconvolution methods assume a space-invariant blur. For a fair comparison, we also applied those algorithms in our space-variant approach by substituting the deconvolution step in the proposed algorithm by those methods to restore each patch of the image.

The PSNR and SSIM metrics for the restored images obtained by the proposed method and the competing algorithms are given in Table 1. The set of kernels also were numerically evaluated using PSNR and the results are shown in Table 2. As an important example, we present the results of applying all methods on the pair of images in Fig. 2c and 1b. The results show that denoising the noisy image is not sufficient to obtain good reconstructions due to the oversmoothing of the small details. We ran `deconvblind` specifying an array of 1's as initial blur, which then defines a uniform blur, as suggested by MATLAB. The resulting blurs, whose numerical results are presented in Table 2, were very poor. We initialized `deconvblind` with the PSF estimates obtained by our method and ran the algorithm for 20 iterations. Results in Table 2 confirmed that `deconvblind` was not able to improve the provided kernel estimates. The restoration results, shown in Fig. 4b and c for the spatially-variant and spatially-invariant approaches, respectively, exhibit strong ringing, more noticeable close to the borders, especially for the spatially-variant approach. The method proposed in [2] provides poor numerical results when applied with the space-variant blur, although the visual quality of

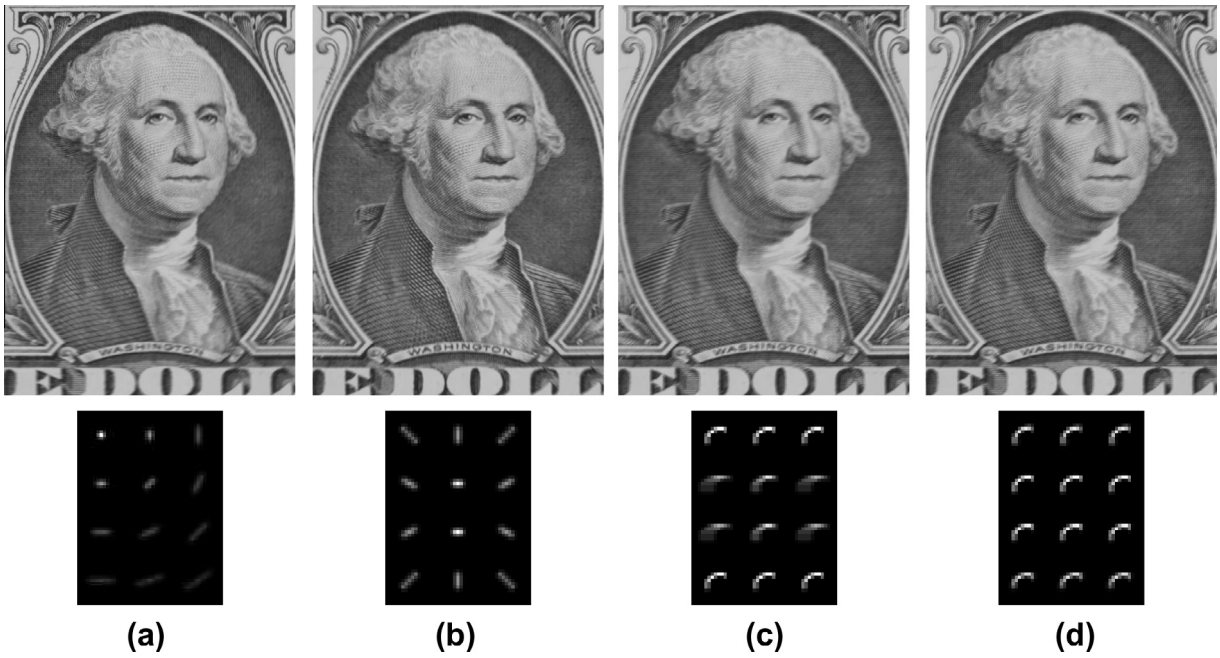

Fig. 2. Blurred images simulating long-exposure shots. The set of PSFs used to generate each image is shown below the corresponding image. The values of the PSFs are mapped to the range [0,255] for visualization purposes.

Fig. 3. Restoration results using the proposed algorithm on the synthetic images in Fig. 2. Top: using the optimal values of λ. Center: using the estimated values of λ. Bottom: Estimated kernels.

Table 1
Peak Signal to Noise Ratio (PSNR) and Structural Similarity (SSIM) figures of merit for the images of the synthetic experiments in Fig. 2.

	Set of blurring kernels							
	a		*b*		*c*		*d*	
	PSNR	SSIM	PSNR	SSIM	PSNR	SSIM	PSNR	SSIM
Blurred	23.88	0.75	23.79	0.75	20.99	0.51	20.80	0.49
Noisy	22.80	0.85	22.80	0.85	22.71	0.85	22.77	0.85
Denoising [23]	24.41	0.89	24.40	0.89	24.07	0.89	24.25	0.89
`deconvblind` (space-var.)	22.95	0.87	21.87	0.88	22.07	0.85	22.10	0.89
`deconvblind` (space-invar.)	22.30	0.78	22.06	0.78	18.76	0.80	18.57	0.83
Method in [2] (space-var.)	17.42	0.74	15.95	0.74	17.76	0.76	19.50	0.82
Method in [2] (space-invar.)	21.65	0.77	21.30	0.77	19.79	0.76	19.63	0.79
Proposed with $\lambda = 0$	25.46	0.85	25.48	0.87	20.51	0.58	20.19	0.56
Proposed with $\lambda = 1$	27.77	0.94	28.49	0.94	27.45	0.93	28.31	0.94
Proposed (estimated λ)	28.26	0.95	29.15	0.95	28.26	0.95	28.74	0.95
Proposed (optimal λ)	28.62	0.95	29.53	0.96	29.08	0.96	30.74	0.97

the images is quite good (see Fig. 4d). This is due to the blur estimation that needs a high amount of data to provide accurate results and provides crisp but noisy results when used on small patches. When this method is used assuming a spatial-invariant blur (Fig. 4e), the results are better but show some staircase effect due to the TV image prior and some ringing appears at patch boundaries due to the spatial-invariant blur assumption. However, it produces very good results when the blur is spatially invariant and needs no user intervention since all the parameters are automatically estimated.

Table 2
Peak Signal to Noise Ratio (PSNR) comparison for the set of kernels estimated in the synthetic experiments.

	Set of blurring kernels			
	a	*b*	*c*	*d*
`deconvblind` (standard initialization)	36.01	84.20	84.67	84.00
`deconvblind` (initialized with our PSF)	57.10	95.09	92.39	91.51
Method in [2]	56.93	89.63	89.10	89.18
Proposed method	57.10	94.99	92.39	91.49

The proposed method with $\lambda = 0$ (i.e., using only the SAR prior model) produces oversmoothed restorations, as can be observed in Fig. 4f. When using only the TV prior model ($\lambda = 1$), the sharp edges are better preserved, as can be seen from the image estimate in Fig. 4g. When λ is estimated, and also when it is adjusted to its optimal value for each block, better results are obtained compared to using a single prior (see, for instance, the texture on the jacket of G. Washington in Fig. 4h).

Table 4 shows the computing times for the experiment on the image in Fig. 2c for the compared algorithms on a Core 2 duo laptop at 2.13 GHz. Note that the current implementation of the

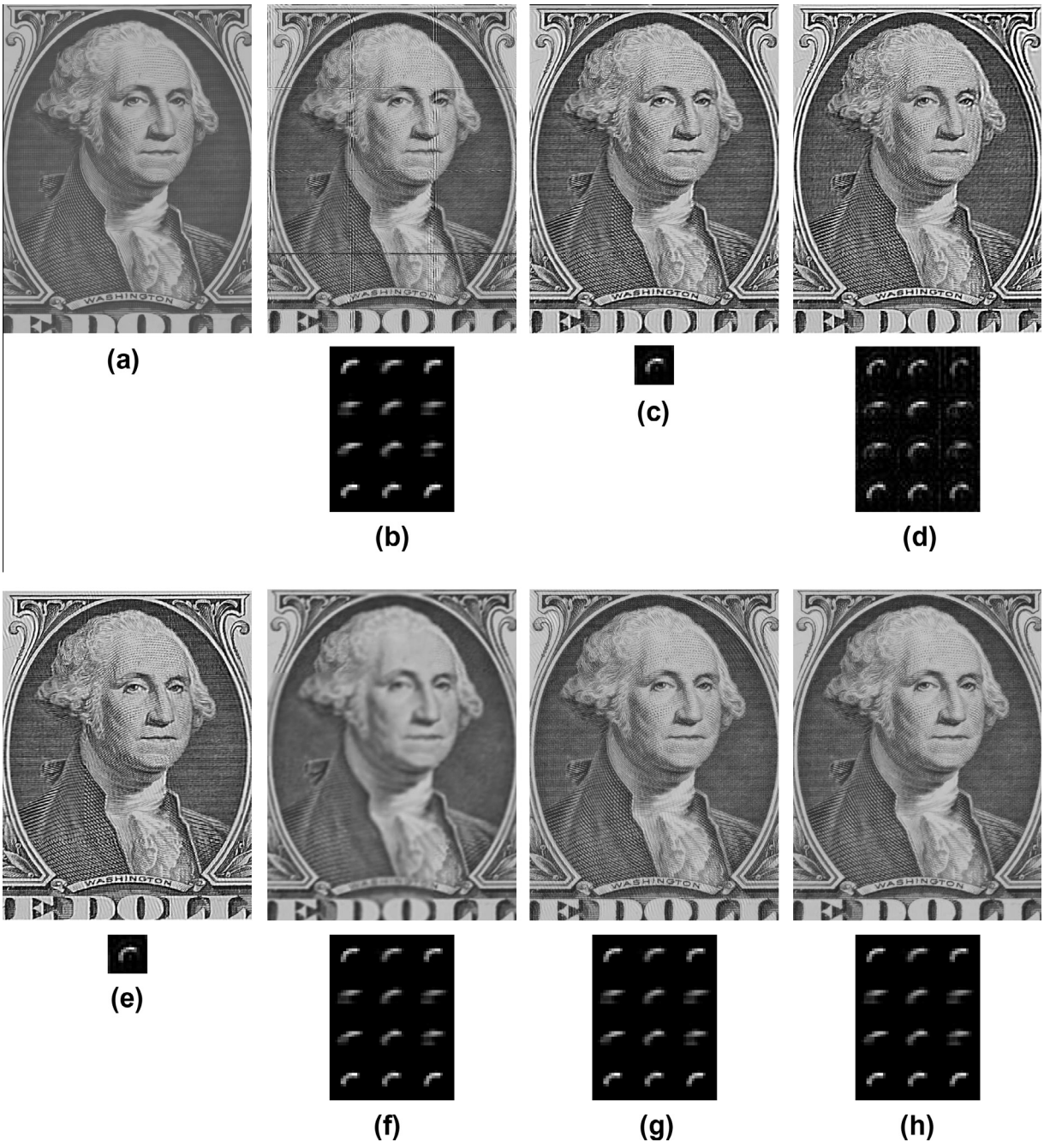

Fig. 4. Restoration results on the synthetic images in Figs. 2c and 1b: (a) denoised image using the method in [23], (b) `deconvblind` assuming a space-variant blur, (c) `deconvblind` assuming a space-invariant blur, (d) method in [2] assuming a space-variant blur, (e) method in [2] assuming a space-invariant blur, (f) proposed method with $\lambda = 0$, (g) proposed method with $\lambda = 1$, (h) proposed method.

Table 3
Optimal (left) and estimated (right) value of λ for each patch of the image in Fig. 2c.

0.6	0.7	0.6
0.8	0.7	0.8
0.6	0.9	0.8
0.6	0.6	0.5

0.5	0.7	0.5
0.8	0.7	0.8
0.5	0.8	0.8
0.5	0.6	0.4

Table 4
Computation time (in seconds) for the experiment on the image in Fig. 2c for the compared method.

Denoising [23]	`deconvblind` (space-var.)	Method in [2]	Proposed
6.9	13.5	326	288

proposed method and the method in [2] are MATLAB non-optimized ones. They could be made faster by utilizing a more elaborated implementation.

Finally, we analyzed the effect of the threshold t on the restoration results. We run the proposed method on the 4 images in Fig. 2 and Fig. 1b considering 7×5 blocks and an overlap of 50%. This implies that 4×3 blocks will have a single blur, since they coincide with the non-overlapping patches in the image. The other blocks will have parts affected by different blurs. In this experiment we show that, when the deconvolution process does not work appropriately for a particular patch (usually due to a poor estimation of the blur in patches affected by different blurs) taking into account only the information from the short exposure image provides better results. The PSNR values when varying t from 1 to 2 are plotted in Fig. 5a for the Fig. 2b. Notice that the curve for the other images had either similar shape or always increased until no block was replaced. For all cases, a value of t between 1.3 and 1.5 provided the best results. We use $t = 1.5$ to give a slightly higher confidence to the deblurred blocks. The PSF estimates are shown in Fig. 5b. Using $t = 1.5$, the image depicted in Fig. 5d is obtained. Note that the four blocks replaced by their denoised version, (Fig. 5c), correspond to blocks affected by different blurs.

In the next set of experiments, we apply the proposed method to three real image pairs acquired in dim environments with different hand-held cameras. The images are depicted in Figs. 6–8a and b. The observed images have been photometrically and geometrically registered as described in Section 2.1. Note that, in our algorithm, histogram equalization is performed only on the luminance band. However, to display Figs. 6b, Fig 7b and Fig. 8b, the chrominance bands of the short-exposure image were also photometrically calibrated using the histogram equalization technique. In all the experiments we used a patch overlap percentage of 50%, *threshold* = 10^{-5} to stop the deconvolution algorithm and a Hann window for the postprocessing step. We compare the proposed algorithm with the state-of-the-art dual exposure image fusion methods presented in [8,7].

The first experiment is conducted on the image pair of size 512×512 depicted in Fig. 6a and b, which was originally published in [9]. This experiment shows the behavior of the proposed algorithm on a scene with object motion and a small camera shake. The exposure time is 1/4 s for the blurred image and 1/15 s with exposure compensation EV −2 for the dim image, and ISO is 400 in both images. Since the blur is not severe, we used a kernel size of 15×15 pixels and 8×8 patches. The estimated kernel for each patch is depicted in Fig. 9a. Patches that cannot be accurately deconvolved, represented in white color in Fig. 9b, are replaced by the corresponding patch of the denoised image by the proposed algorithm. Note that the algorithm deconvolved correctly some patches with moving objects, as the children on the right hand side of the image in Fig. 6a, since it prioritized the information from the noisy observation. The resulting image, displayed in Fig. 6f, presents a higher contrast than the denoised image in Fig. 6c with no background noise, more realistic results than the obtained ones with the method in [2] (see, the man and the child on the bikes at the left hand side of the image distorted due to spatially variant blur) and slightly better details than the image restored with the method in [8], depicted in Fig. 6e (see, for instance, the tree in the background).

The second experiment, conducted on the image pair of size 512×512 shown in Fig. 7a and b, shows the performance of the algorithm in situations with a severe motion blur and a high level of noise in the short-exposure image. The exposure time for the blurred image is 1.3 s at ISO 100 and 1/100 s at ISO 400 for the dim image. The number of blocks is set to 6×6, with a kernel size of 47×47. The noise in the calibrated short exposure image is so severe that denoising only helps to recover some details around the cup where noise is less noticeable (see Fig. 7c). The method in [2] (Fig. 7d) did not provide a good estimate of the kernel due to the large smooth areas in the image and the restored image is oversmoothed The restored image obtained by the method in [8], shown in Fig. 7e, recovered the image details around the cup and the vase. However, it oversmoothed both objects and produced some false contours at the bottom of the vase, and the background is noisier and dimmer than the image obtained by the proposed method, which is shown in Fig. 7f. The proposed method accurately deconvolved the vase and the books behind it, thanks to the estimation

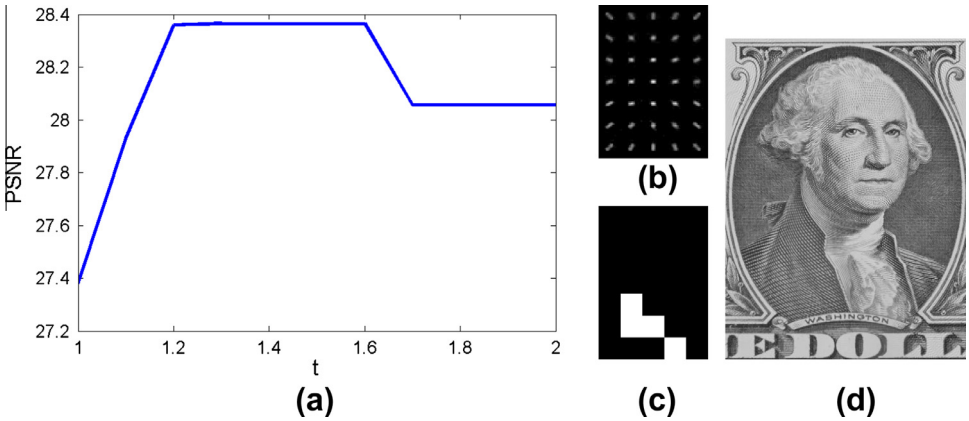

Fig. 5. (a) PSNR evolution for different values of t using the estimated values of λ. (b) Estimated PSF. (c) Denoised patches with $t = 1.5$. (d) Restored image with $t = 1.5$.

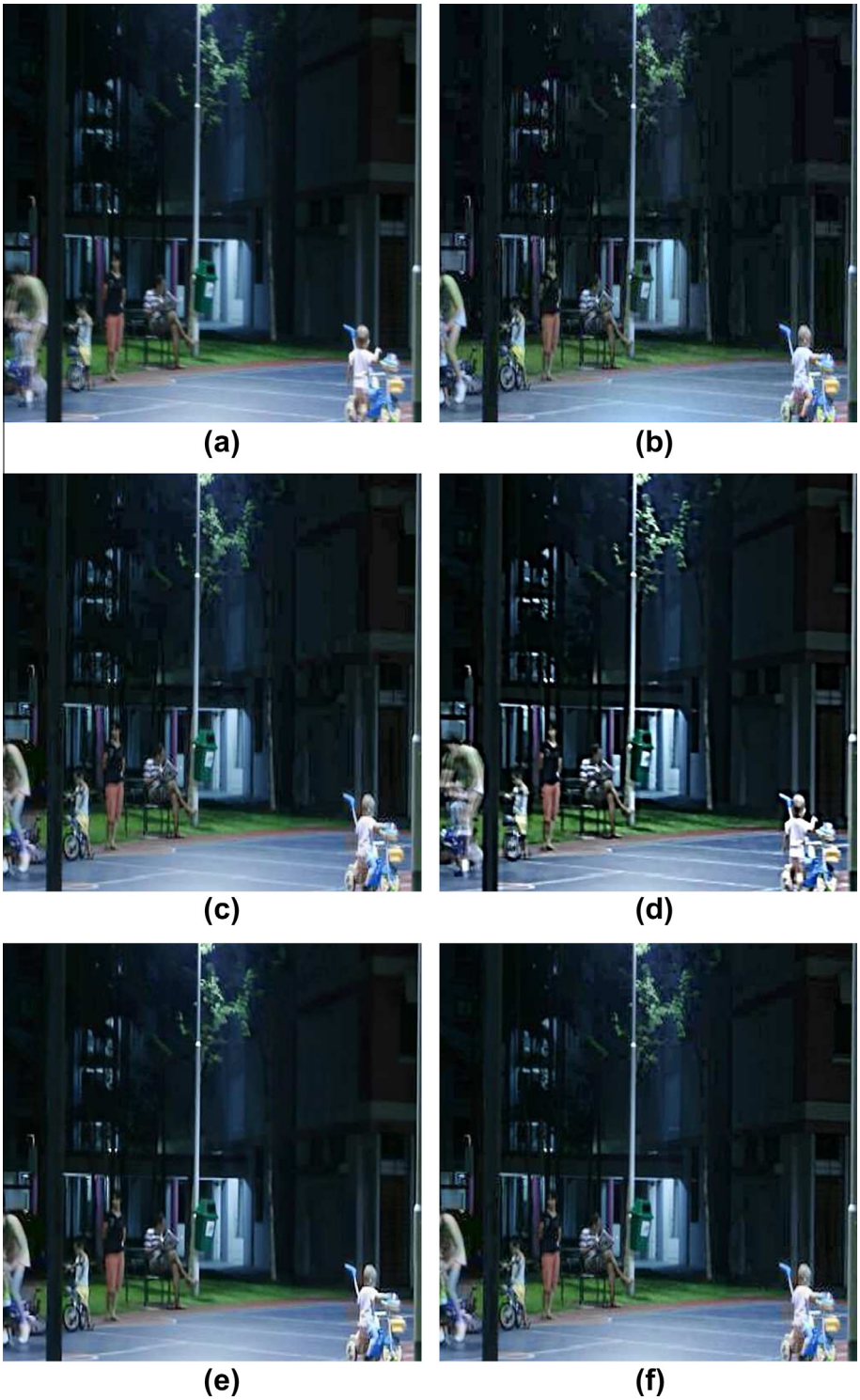

Fig. 6. (a) Observed long-exposure image and (b) observed short-exposure image, (c) denoised image using [23], (d) restored image with the method in [2], (e) restored image with the method in [8] and (f) restored image with the proposed method.

of the blur that is able to recover the small rotation of the camera during the capture process (see Fig. 9c). It can be seen that the method preferred the denoised version of the blocks around the vase area (Fig. 9d) instead of the deconvolved ones. Note that small details such as the letters in the cup or in the book behind the vase are now visible, and the reflections in the vase are recovered.

The last experiment is performed on the image pair of size 800×600 depicted in Fig. 8a and b. This long exposure image exhibits two types of blur, one due to global camera shake and one produced by a reduced depth of field (DOF). The exposure time in the blurred image is 1/10 s and 1/160 s with exposure compensation EV -4 for the dim image, and ISO is 100 with both images. We used a kernel size of 31×31 pixels and 8×6 patches. The short-exposed image in Fig. 8b contains a strong level of quantization noise that is not eliminated by denoising as shown in Fig. 8c. The restoration by the proposed method (Fig. 8f) is much sharper

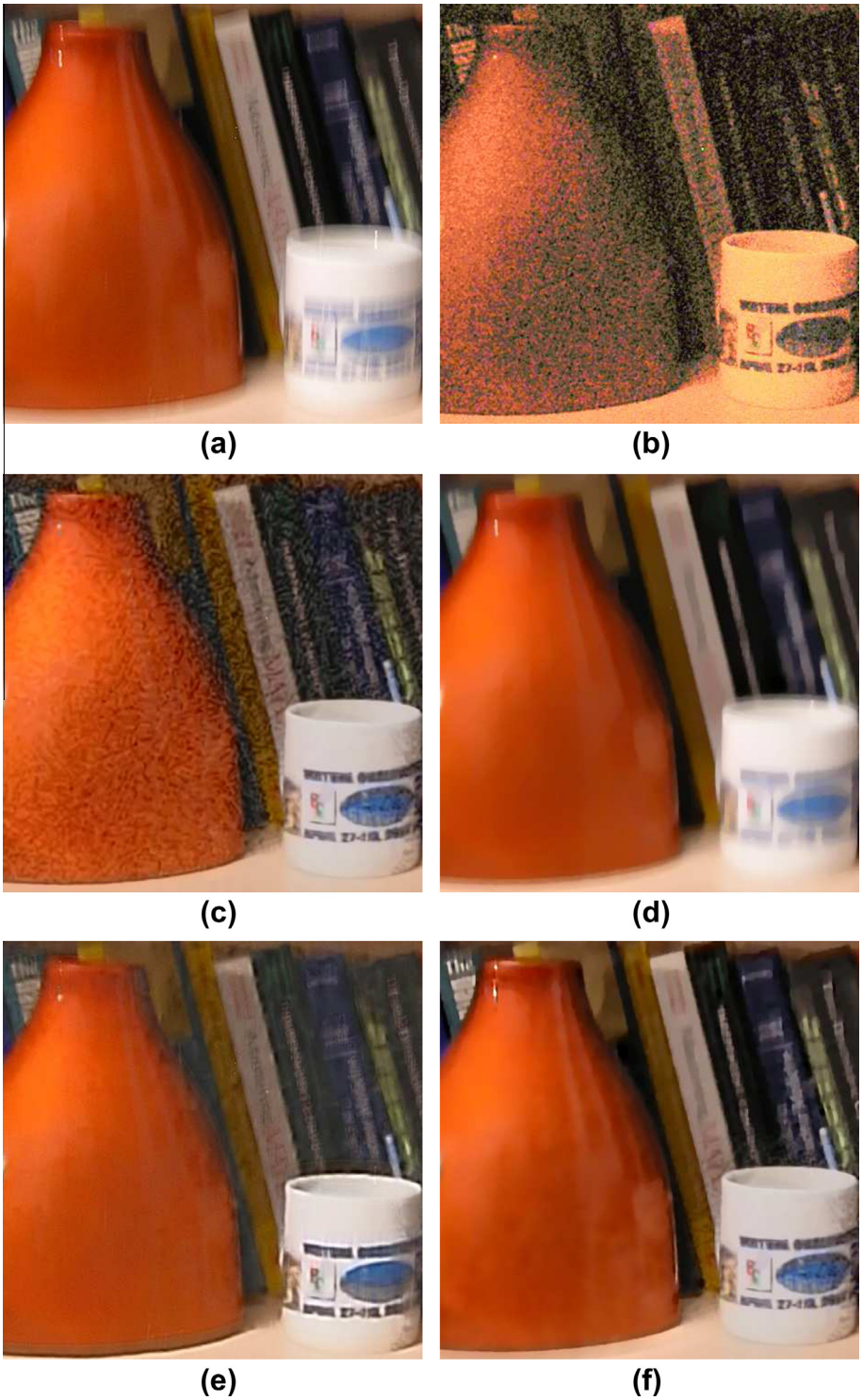

Fig. 7. (a) Observed long-exposure image and (b) observed short-exposure image, (c) denoised image using ([23]), (d) restored image with the method in [2], (e) restored image with the method in [8] and (f) restored image with the proposed method.

image than the image obtained by [7] (Fig. 8e) and [2] (Fig. 8d). The proposed method solves the reduced depth of field problem and replaces the bright streetlamp in the front by its denoised version. Notice that it was not possible to obtain a good kernel estimate in the blocks around the bright streetlamp due to saturation, and our method correctly decides to use denoising in these areas. Denoising was also chosen in the area with the trees and the wall with two different blurs due to different depths (see Fig. 9f for the decision map).

4. Discussion and conclusions

In this paper we proposed a method to restore blurred images taken in dim environment with the help of a short-exposure sharp

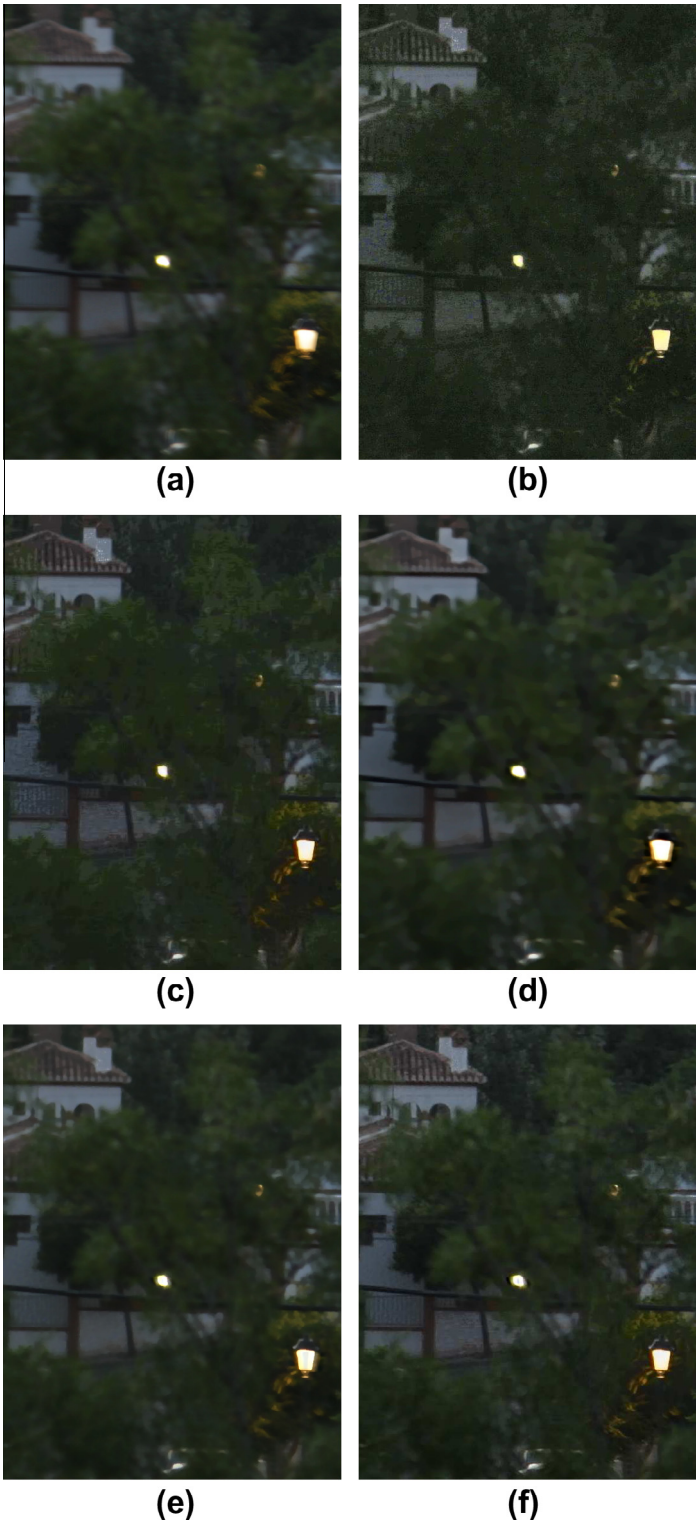

Fig. 8. (a) Observed long-exposure image and (b) observed short-exposure image, (c) denoised image using [23], (d) restored image with the method in [2], (e) restored image with the method in [7] and (f) restored image with the proposed method.

but noisy image. The developed algorithm can be applied to both camera shake and object motion blur, since it employs a space variant kernel estimation by utilizing the noisy image. The proposed method is also suitable in case of reduced depth of field. The method minimizes blur artifacts and noise propagation in the recovery process. We have shown that, using a combination of prior models into the hierarchical Bayesian paradigm, the proposed restoration method provides better results than the method using only a TV prior, producing an image with better texture while preserving sharp edges. In addition, the parameters in the image estimation step are automatically estimated without the need for user intervention. Future work will include the use of dynamic patch size and to incorporate the estimation of the parameter λ into the Bayesian formulation.

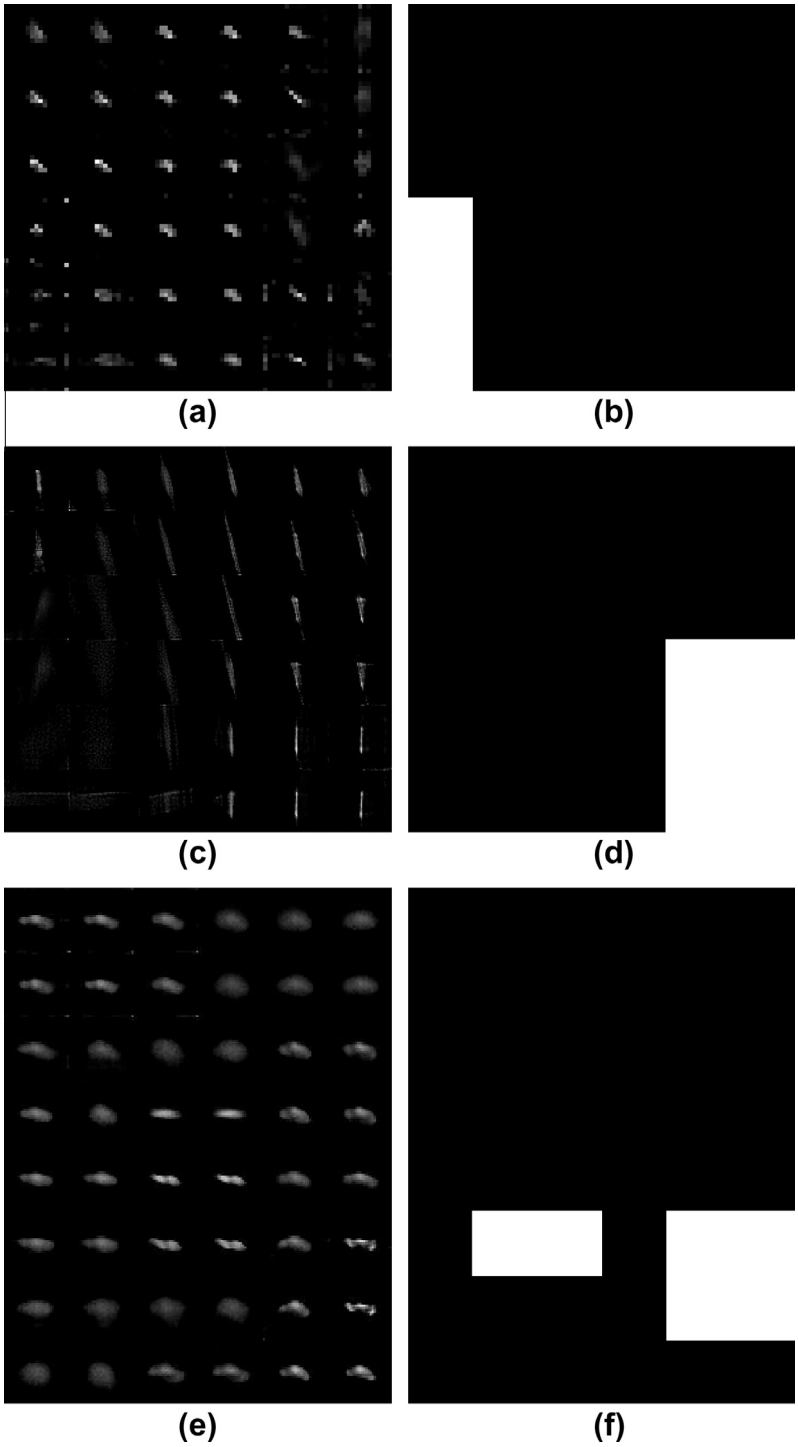

Fig. 9. Estimated kernels and selection strategy for each real experiment. Patches in white represent patches where denoising was applied. The values of the PSFs are normalized to the range [0,255] for displaying purposes. (a) Obtained kernels for the images in Fig. 6a and b. (b) Selection strategy for the restoration in Fig. 6f. (c) Obtained kernels for the images in Fig. 7a and b. (d) Selection strategy for the restoration in Fig. 7f. (e) Obtained kernels for the images in Fig. 8a and b. (f) Selection strategy for the restoration in Fig. 8f.

Acknowledgements

The authors thank M. Tico and M. Sorel for providing the real image sets for the first and second experiments and the results of their methods. This work was supported in part by the "Ministerio de Ciencia e Innovación" under Contract TIN2010-15137 and by a grant from the U.S. Department of Energy (DE-NA0000457).

References

[1] L. Yuan, J. Sun, L. Quan, H.-Y. Shum, Image deblurring with blurred/noisy image pairs, ACM Trans. Graph. 26 (3) (2007) 1.
[2] S.D. Babacan, J. Wang, R. Molina, A.K. Katsaggelos, Bayesian blind deconvolution from differently exposed image pairs, IEEE Trans. Image Process. 19 (11) (2010) 2874–2888.
[3] M. Tallón, J. Mateos, S.D. Babacan, R. Molina, A.K. Katsaggelos, Combining observation models in dual exposure problems using the Kullback–Leibler divergence, in: European Signal Processing Conference (EUSIPCO), 2010, pp. 323–327.

[4] E. Kee, S. Paris, S. Chen, J. Wang, Modeling and removing spatially-varying optical blur, in: Proc. IEEE Int. Conf. of Computational Photography (ICCP), 2011, pp. 1–8.
[5] O. Whyte, J. Sivic, A. Zisserman, J. Ponce, Non-uniform deblurring for shaken images, in: Proc. IEEE Conf. Computer Vision and Pattern Recognition (CVPR), 2010, pp. 491–498.
[6] M. Šorel, F. Šroubek, Space-variant deblurring using one blurred and one underexposed image, in: Proc. IEEE Int. Conf. on Image Processing (ICIP), 2009, pp. 157–160.
[7] M. Šorel, F. Šroubek, J. Flusser, Towards super-resolution in the presence of spatially varying blur, in: M. Peyman (Ed.), Super-resolution Imaging, CRC Press, 2010, pp. 187–218 (Chapter 7).
[8] M. Tico, K. Pulli, Image enhancement method via blur and noisy image fusion, in: Proc. IEEE Int. Conf. on Image Processing (ICIP), 2009, pp. 1521–1524.
[9] M. Tico, N. Gelfand, K. Pulli, Motion-blur-free exposure fusion, in: Proc. IEEE Int. Conf. on Image Processing (ICIP), 2010, pp. 3321–3324.
[10] N. Cvejic, T. Seppanen, S.J. Godsill, A nonreference image fusion metric based on the regional importance measure, IEEE J. Select. Top. Signal Process. 3 (2) (2009) 212–221.
[11] M. Tallón, J. Mateos, R. Molina, A. Katsaggelos, Image prior combination in space-variant blur deconvolution for the dual exposure problem, in: 7th International Symposium on Image and Signal Processing and Analysis (ISPA), 2011, pp. 408–413.
[12] R.C. Gonzalez, R.E. Woods, Digital Image Processing, Prentice Hall, 2008.
[13] H. Bay, T. Tuytelaars, L.V. Gool, Surf: speeded up robust features, in: European Conf. on Computer Vision (ECCV 2006), 2006, pp. 404–417.
[14] M.A. Fischler, R.C. Bolles, Random sample consensus: a paradigm for model fitting with applications to image analysis and automated cartography, Commun. ACM 24 (6) (1981) 381–395.
[15] R.I. Hartley, A. Zisserman, Multiple View Geometry in Computer Vision, second ed., Cambridge University Press, 2004.
[16] M. Tallón, J. Mateos, S. Babacan, R. Molina, A. Katsaggelos, Space-variant kernel deconvolution for dual exposure problem, in: European Signal Processing Conference (EUSIPCO), 2011, pp. 1678–1682.
[17] S.D. Babacan, R. Molina, A. Katsaggelos, Parameter estimation in TV image restoration using variational distribution approximation, IEEE Trans. Image Process. 17 (3) (2008) 326–339.
[18] B.D. Ripley, Spatial Statistics, John Wiley, 1981.
[19] M. Vega, J. Mateos, R. Molina, A. Katsaggelos, Astronomical image restoration using variational methods and model combination, Stat. Methodol. 9 (1–2) (2012) 19–31.
[20] S. Villena, M. Vega, R. Molina, A.K. Katsaggelos, Image prior combination in super-resolution image reconstruction, in: European Signal Processing Conference (EUSIPCO), 2010, pp. 616–620.
[21] J.-L. Starck, M. Elad, D.L. Donoho, Image decomposition via the combination of sparse representations and a variational approach, IEEE Trans. Image Process. 14 (10) (2005) 1570–1582.
[22] S. Kullback, Information Theory and Statistics, Dover Publications, New York, 1959.
[23] K. Dabov, A. Foi, V. Katkovnik, K. Egiazarian, Image denoising by sparse 3-D transform-domain collaborative filtering, IEEE Trans. Image Process. 16 (8) (2007) 2080–2095.
[24] M. Hirsch, S. Sra, B. Scholkopf, S. Harmeling, Efficient filter flow for space-variant multiframe blind deconvolution, in: Proc. IEEE Conf. Computer Vision and Pattern Recognition (CVPR), 2010, pp. 607–614.
[25] P.E. Debevec, J. Malik, Recovering high dynamic range radiance maps from photographs, in: Proc. 24th Annual Conf. on Computer Graphics and Interactive Techniques (SIGGRAPH), 1997, pp. 369–378.